Stress Intensity Factor in Top-loaded Thin Hemispherical Domes: A Combined Experimental and Numerical Study

Siwen Cao[1], Yu Zhang[2]*

[1] Department of Structural Mechanics, Faculty of Civil Engineering, Budapest University of Technology and Economics, Műegyetem rkp. 3., H-1111 Budapest, Hungary
[2] Department of Industrial Engineering, University of Padua, Via Gradenigo, 6/a, 35131 Padua, Italy
* Corresponding author, e-mail: yu.zhang@phd.unipd.it

Abstract

Measuring the stress intensity factors (SIF) at the tip of the meridian cracks of a dome can help evaluate the fracture process. The calculation of the SIF for planar cracks, based on truncating the Williams' series expansion, can be extended to curved surface cracks using the equivalent plane transformation method. This study investigates the effects of dimensions, crack length, and distributed loading area on the SIF at the crack tip, both experimentally and numerically. The results show that dimensionless SIFs generally increase with the crack length, distributed loading area and thickness ratio (thickness/ radius). The distribution load prevents any tension within the contact zone and suppresses top-surface radial cracking. The effect becomes more pronounced as the model thickness increases. Within the bearing capacity limits, designing a wide loading edge can effectively inhibit the propagation of meridian cracks and increase the service life of the dome.

Keywords

thin hemispherical dome, stress intensity factor, simulation, experiment

1 Introduction

The maintenance of building structures is crucial for preserving their integrity and ensuring long-term use. Accurate assessment helps find issues and gives effective measures. Zavvar, et al. [1–4] analyzed stress concentrations under different loads with numerical simulations. Meanwhile, Ahmadi, et al. [5–8] derived parameterized formulas to characterize stress concentrations for different conditions. Domes are commonly used in ancient buildings, those long-span structures, often built from masonry and concrete, are susceptible to cracking due to their limited tensile strength. St. Peter's Church. [9, 10] and similar ancient buildings develop cracks of varying degrees as their domes age. Evaluating and repairing cracks in domes remains a challenging problem, and requires sophisticated mechanical and mathematical models [11–13].

The stress intensity factor (SIF) is a common parameter to describe the stress intensity at crack tips and can be used to determine the crack growth [14, 15]. Experimentally, the on-planar SIF can be calculated with the Williams' series [16–18] For non-planar SIF of cracks

on shell structure, Vormwald, et al. [19, 20] assumed thin-walled cylindrical shells as flat surface to determine SIF, but this approach is too crude and introduces large errors. Additionally, Camacho-Reyes [21] gives a differential geometry method based on the 3D-DIC for crack tip field characterization on non-planar (curved) surfaces, but it is limited to surfaces with zero Gaussian curvature. More recently, Cao and Sipos [22] proposed a method for calculating the SIF of cracks on surfaces with non-zero Gaussian curvature, such as domes. This method makes it possible to obtain the SIF of cracks on domes. Therefore, this method was adopted in this study.

In this paper, the evolution of crack tip SIF is obtained by experiments and numerical simulations. The effects of geometry (dome thickness and crack length) and loading (top axial loading area) on the dimensionless SIF are considered. Results can be referenced when designing and building a dome. After the crack length is detected and the load is estimated, the SIF at the crack tip can be obtained by interpolating the results of this paper.

2 Methodology

The calculation of the SIF for planar cracks, based on truncating the Williams' series expansion, can be extended to curved surface cracks using the equivalent plane transformation method [22]. Furthermore, the SIF can be calculated for meridian cracks in thin-walled hemispherical domes.

The evolution of crack tip SIF is obtained by experimentally using top-distributed loading of dome specimens containing prefabricated cracks. In the experiments, we considered the effects of prefabricated crack length and distributed loading area on crack tip SIF.

We also conducted numerical simulations under the same parameter conditions to make the results more referenceable. In the numerical simulation, we considered the effects of crack length, distributed loading area and dome thickness on the crack tip SIF.

In this work, as Fig. 1 shows, we use loading apex angle θ denotes distributed loading area, the center angle of the crack φ denotes crack length.

3 Experiment

3.1 Specimen fabrication

PMMA is a commonly used material in structural experiments. Ewing and Williams [23] studied the behavior of spherical PMMA shell under pressure, while Liu et al. [24] investigated the stress singularity at the crack tip of PMMA cylindrical shells. Qasim et al. [25] tested the margin cracking of hemispherical PMMA shells under top-loading conditions. Compared to rock and cement, PMMA is an ideal homogeneous material, offering better experimental consistency.

As Fig. 2 shows, thermos-molding is an efficient method for fabricating a hemispherical shell. The PMMA plate is heated until it becomes soft and is held in place by two up-and-down fixers. The upper fixer contains a hole with the radius of the target hemispherical shell. By blowing pressurized gas into the gap between the lower fixer and the PMMA plate, the plate is molded to the desired shape. After cooling down and cutting, a hemispherical PMMA dome is fabricated. Meanwhile, the material properties are tested using a uniaxial tensile test on a PMMA plate from the same batch. The results are shown in Table 1.

3.2 Experiment processing

As shown in Fig. 1, the specimen has an inner radius R of 100 mm and a thickness h of 5 mm, and it is compressed by uniaxial force. The loading conditions significantly influence the location and propagation direction of the cracks. Generally, the point contact between the hard indenter and
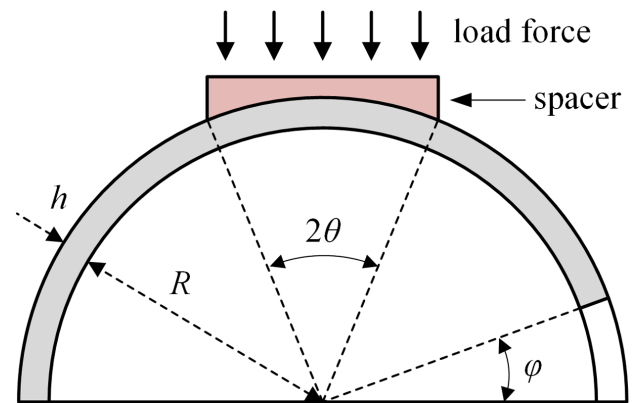

Fig. 1 dimensions of specimen and the defination of the loading apex angle θ and the center angle of the crack φ
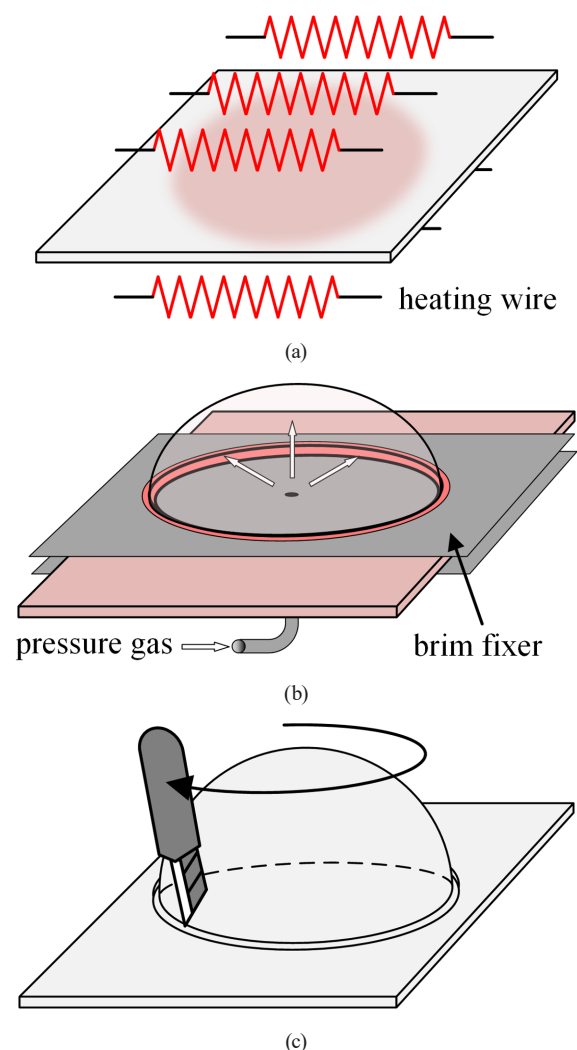

Fig. 2 Thermomoulding of PMMA dome specimens (a) heating the PMMA plate; (b) moulding PMMA by pressure gas; (c) cutting

Table 1 The material properties of PMMA

Material	Modulus of elasticity E [MPa]	Poisson's ratio v
PMMA	1200	0.37

the top of the dome tends to generate radial cracks originating from the apex [25]. The distributed load, however, prevents tension within the contact zone and suppresses radial cracking on the top surface [26]. In this study, the loading force is distributed by the spacer, whose size is determined by the contact surface apex angle θ. For different loading conditions, the apex angle θ is set to 20°, 30° and 40°, respectively.

Meanwhile, the pre-existing crack is created by the diamond wire saw, and the length of the crack is denoted by the corresponding crack center angle φ. The crack center angles φ used in the experiment are 10°, 15°, 20°, 25°, and 30°. As shown in Fig. 3, domes were loaded vertically along their axis of symmetry (Zwick/Roell Z-150 testing machine of the Adolf Czakó Laboratory at the Budapest University of Technology and Economics) with a loading speed of 0.25 mm/min. Vaseline was greased between the bottom of the dome and the plate to reduce friction, and the displacement fields during loading were recorded using the Correlation Solutions VIC-3D system for the next processing.

3.3 Post-processing
In this study, the 3D-DIC system utilizes VIC-Snap – VIC-3D the software [27] (designed by Correlated Solutions, Columbia, SC, US), along with a two-camera and illuminator set-up. Two digital cameras, each equipped with a pair of FUJINON (HF75SA-1) lenses with adjustable focal length, provide the required resolution and accuracy. As shown in Fig. 3, a white light source illuminated the specimen's surface during testing. The deformed images were correlated with the unloaded image to obtain the displacement fields. The captured images had a semicircular region with a radius of 800 pixels with an 8-bit depth.
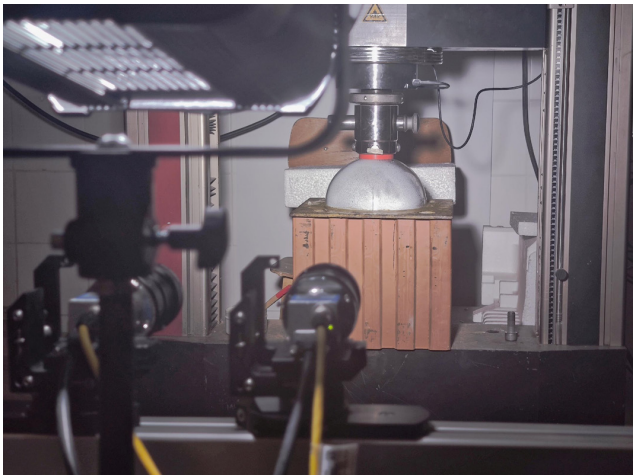

Fig. 3 A specimen placed into the testing machine

In this study, a subset size is 11×11 pixels, with an accuracy of 0.02 pixels. Additionally, the crack tip is visually identifiable in the current study. Fig. 4 shows the U, V, and W displacements on the specimen's surface.

To calculate the SIF of a curved shell, the displacements on the curved shell must first be projected on a plane. As shown in Fig. 5, the equivalent planar of thin shell (tangent plane) is located at the crack tip. The vector k denotes the unit normal vector of the surface at the crack tip, The vector i denotes the unit vector in the tangent plane, directed along the extended crack, set $j = k \times i$, where '$\times$' denotes the cross product. The displacement vectors U, V, and W in the global coordinate system (x, y, z) can be projected to the local coordinate system (i, j, k) via:

$$\begin{bmatrix} u \\ v \\ w \end{bmatrix} = A_{(x,\ y,\ z)\to(i,\ j,\ k)} \begin{bmatrix} U \\ V \\ W \end{bmatrix},$$ (1)

where matrix A $(x, y, z) \to (i, j, k)$ is the transformation matrix, u, v, w are the displacement vectors in basis (i, j, k). The component w direct along k spanned by i and j, which means the 2D displacement components are vectors u, v.

It should be noted that u and v cannot be used directly to calculate SIF, as ignoring w would be unreasonable. Here, we aim to take w and the curvature R of the curved shell into account when obtaining an equivalent plane that contains the displacement. Following the lead of [22] we introduce two assumptions:

1. the distribution of w in basis (i, j, k) is close to linear around the crack tip; hence.

$$w \cong ax + by + c,$$ (2)

where the constants (a, b, c) can be obtained from the measurements via a least-square fit.

2. close to the crack tip, the surface is a paraboloid, in case of spherical specimens,

$$W(x,\ y) = -\frac{1}{2R}x^2 - \frac{1}{2R}y^2,$$ (3)

respectively. Where $W(x, y)$ in global basis (x, y, z) denotes the midsurface of the shell in the unloaded state.

In the case of a shell with moderate curvature, the classical Föppl-von Kármán (FvK) shell equations can be readily extended [28, 22]. To satisfy the extension, the displacements $(\bar{u}, \bar{v})$ on the equivalent plane should read:

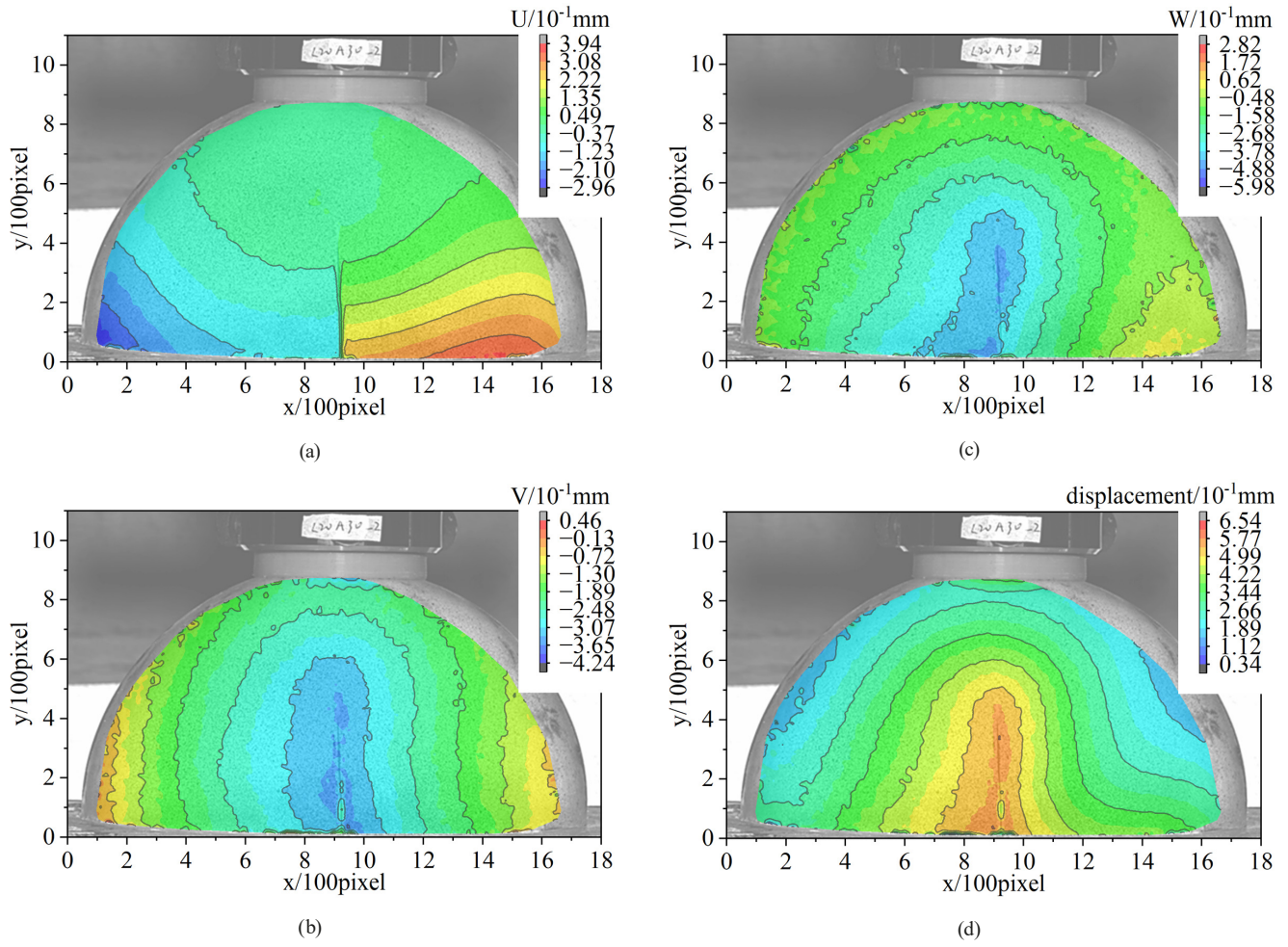$$\bar{u} = u + aW(x,\ y) + \frac{1}{2}a^2 x + \frac{1}{2}aby,$$ (4)

Fig. 4 *U*, *V*, and *W* displacement on the surface of a specimen displacement field observed by DIC on the surface of a specimen (a) *U* displacement; (b) *V* displacement; (c) *W* displacement; (d) total displacement
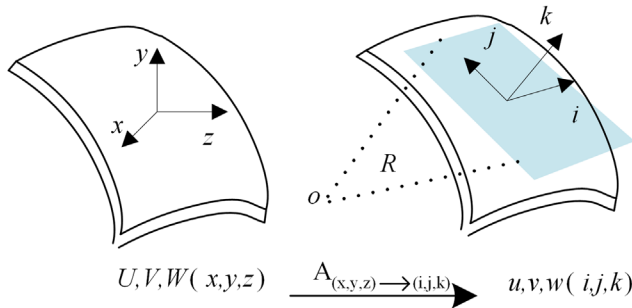

Fig. 5 Projection of the displacements on the tangent plane

$$\overline{v} = v + bW(x, \ y) + \frac{1}{2}b^2 y + \frac{1}{2}abx. \tag{5}$$

U, *V*, and *W* can be obtained from measurements, The values for *u*, *v*, *w* and be calculated by Eq. (1), *w* is used to determine a plane and constants (*a*, *b*, *c*). The equivalent displacements $(\overline{u}, \ \overline{v})$ can be calculated on the equivalent planar of thin shell. Then, the SIF can be calculated via the 2D William's expansion [17].

4 Simulation

As shown in Fig. 6 (a), the model generated by ABAQUS is similar to the experimental setup. The radius *R* of the hemispherical shell model is 100 mm, the thickness *h* varies within the range of *R*/10, *R*/20, *R*/30. The top loading has an apex angle *θ* of 20°, 25°. 30°, 35°, 40°, while the crack center angle *φ* is set to 10°, 15°, 20°, 25°, 30°. The material properties of the model are the same as those of the experimental material, as listed in Table 1. As Fig. 6 (a) shows, the top loading is a distributed load, the load force *P* is applied at the load control point at the top of the numerical model, and the load control point binds (binding type: Kinematic at all degrees of freedom) with the load surface to apply the load force to a distributed loading, the loading force increases linearly over time from 0 N to 1,000 N. and the boundary condition to the bottom of the model is that all degrees of freedom except the *x* and *y* direction are constrained at the bottom of the model.
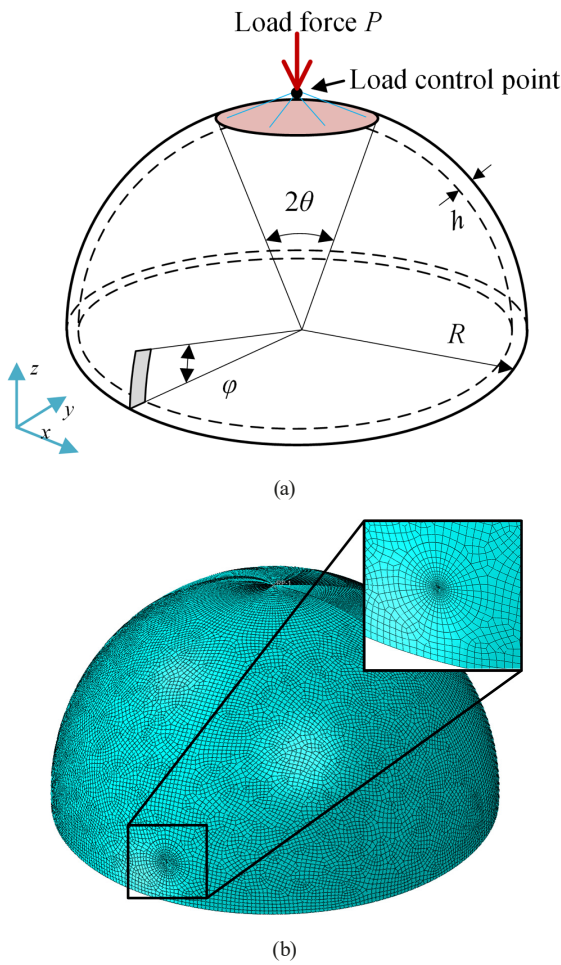
(a)

(b)

Fig. 6 Simulation model (a) model dimensions, boundary conditions and loading set-up; (b) meshing of model, the meshing at the crack tip is enlarged for better clarity

The mesh of the model shown in Fig. 6 (b) uses the element type C3D20R (20-node quadratic brick reduced integration element) surrounding the crack tip, while the rest of the model uses the element type is C3D8R (8-node linear reduced integration element). Since the thickness of the numerical model varies, the typical size of the element is set to 1/4 of the thickness h of the model. The region surround the crack tip is meshed with a finer mesh to improve the precision of the stress singularity.

Moreover, as shown in Fig. 7, for the C2D20R element surrounding the crack tip, moving the midside node toward to the crack tip can also increase the accuracy of the stress intensity factors calculation. Generally, to set the singularity for an elastic fracture, the midside node parameter should be 0.25 near the crack tip. For shell structure models, the midside node parameter should be greater than 0.25 but less than 0.5 to avoid the element Jacobian from becoming negative [29]. Therefore, the midside node parameter is set to 0.3 for all simulation.
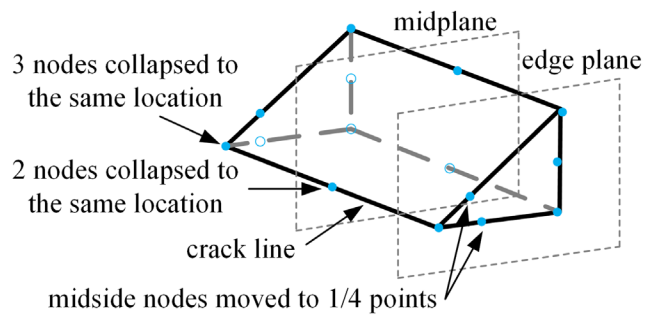

Fig. 7 Setting of the singularity at the crack tip C3D20R element [29]

The inner function in ABAQUS used to calculate the SIF requires the number of contours surrounding the crack tip. The first layer of elements surrounding the crack tip is used for the first contour integral to calculate the SIF, and additional layers of elements are used for the subsequent contours. In this study, the number of contours is set to 10. Fig. 8 shows the SIF K_1-contour number series plot of an element at the crack tip. K_1 at the small contour deviates from K_1 of other contours, which is consistent with the suggestion in ABAQUS manual [29]. Considering the singularity at the crack tip, for linear elastic simulation, the SIF results from the first and second contour should be excluded for better accuracy.

5 Results

From both the experiment and simulation, the results can be obtained. For better comparison and to avoid the influence of structure dimension, as shown in Eq. (1), it is common to calculate the SIF as its corresponding dimensionless SIF F (also known as the normalized SIF) [30–32].

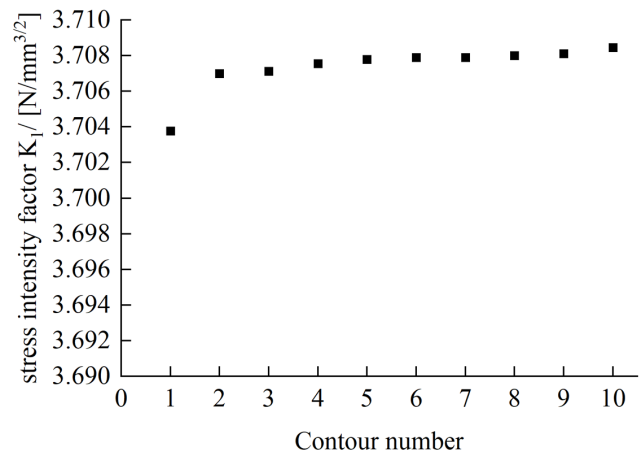$$F = K_1 / \sigma \sqrt{\pi a}, \tag{6}$$

Fig. 8 Stress intensity factor K_1 for different contour for model with 20° loading apex angle and 10° crack center angle

where, K_1 is the stress intensity factor for model 1 (opening) cracking, $\sigma = P/(\pi R^2 \sin^2\theta)$, P is the amount of loading force, R is the radius of structure, θ is the half of loading area apex angle, $a = R\varphi$ is the length of crack, and φ is the center angle of crack.

Generally, the dimensionless SIF can be described as the function of material properties (elastic modulus E, Poisson's ratio v), dimensions (thickness ratio h/R), and others (crack center angles φ, loading apex angle θ, and etc.) [33]. As shown in the format, the dimensionless SIF in this study is defined as the function of dimensions, crack center angle, and loading apex angle only.

$$F = f\left(h/R,\ \varphi,\ \theta\right). \tag{7}$$

Fig. 9 shows both experimental and numerical dimensionless SIFs for comparison, as φ increases, the dimensionless SIF increases. Specifically: when $\theta = 20°$, the dimensionless SIF $\in [0, 10]$; when $\theta = 30°$, the dimensionless SIF $\in [5, 15]$; when $\theta = 40°$, the dimensionless SIF $\in [10, 20]$, the results from experiments and simulations can match well. Detailly, When $\theta = 20°$ (Fig. 9 (a)), the dimensionless SIF from the numerical simulation increases monotonically, and the dimensionless SIF from the experiment almost coincides with that of the numerical simulation. And for loading apex angle $\theta = 30°$ and $40°$, they show the same trend, but the increasing trend decreases for $\theta = 30°$ (Fig. 9 (b)), $\varphi = 25°$, and the curve of simulation decreases for $\theta = 40°$ (Fig. 9 (c)), $\varphi = 20°$.

As Table 2 given, the percentage of relative differences between the experiment to simulation dimensionless SIF, the difference is small when the crack center angle φ is small and big when at the crack center angle $\varphi = 30°$, As shown in Fig. 10, the contact diagram between the specimen and the spacer, The friction between the gasket and the specimen is limited, compared with the top loading method (Fig. 6 (a)) of the numerical simulation model, the constraint effect of the top load on the crack close to the loading edge in the experiment is lighter than that under the numerical simulation conditions, specifically, when the crack tip is less than 40° from the loading edge, the stress field near the crack tip is affected. Fig. 11 provides a good example: the stress contour of the model with $\theta = 40°$ and $\varphi = 30°$ shows that the crack tip is close to the loading edge, and the influence from the loading edge affects the stress field surrounding the crack tip.

To fully analysis how the dimensions, θ, and φ affect the dimensionless SIF, the results of simulations with different thickness ratio are shown in Figs. 12, 13, and 14, corresponding to the models with thickness ratio
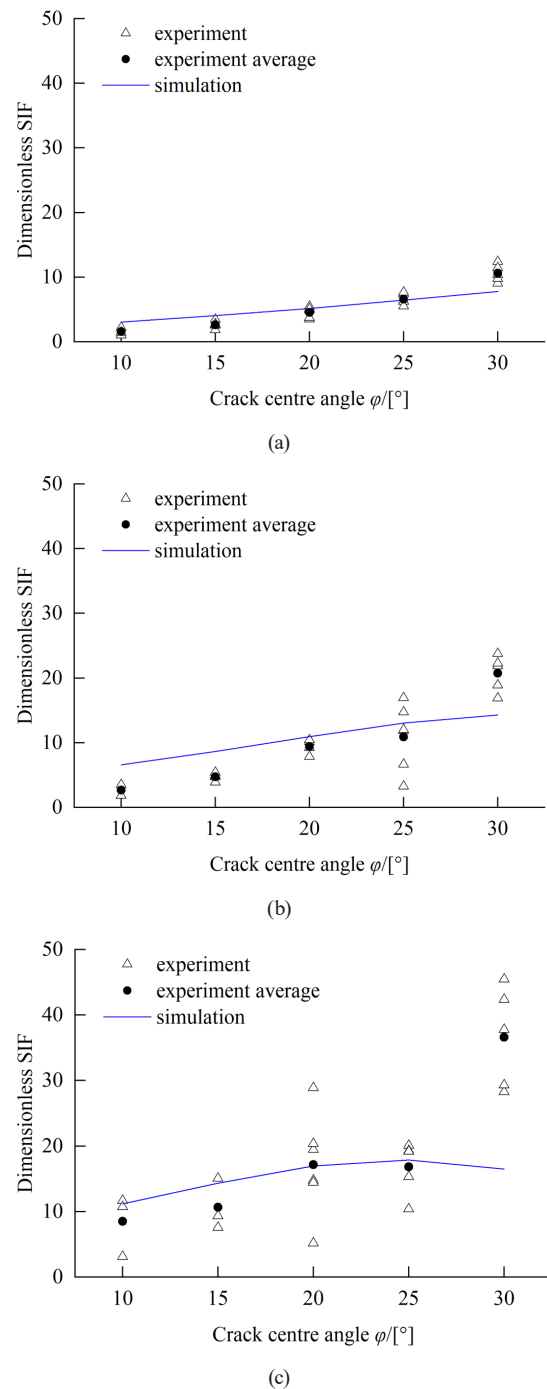

(a)

(b)

(c)

Fig. 9 Comparison of dimensionless SIF results of simulation and experiment (a) loading apex angle $\theta = 20°$; (b) loading apex angle $\theta = 30°$; (c) loading apex angle $\theta = 40°$

Table 2 The percentage of relative differences between the experiment to simulation dimensionless SIF [%]

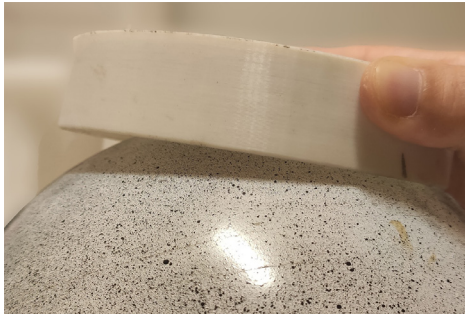| loading apex angle θ [°]	Crack center angle φ [°]				
	10	15	20	25	30
20	49.18	34.61	12.72	1.93	35.64
30	59.69	45.66	14.00	16.58	44.95
40	23.97	25.80	1.14	5.91	122.38

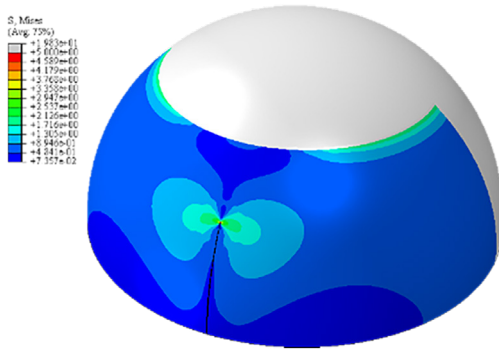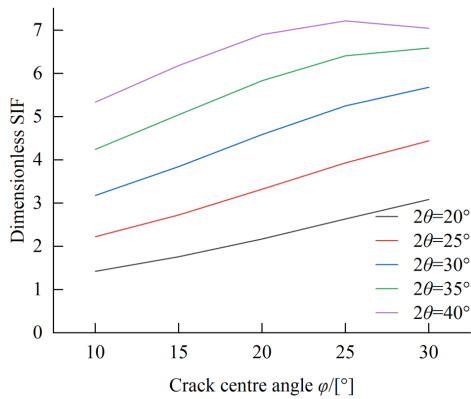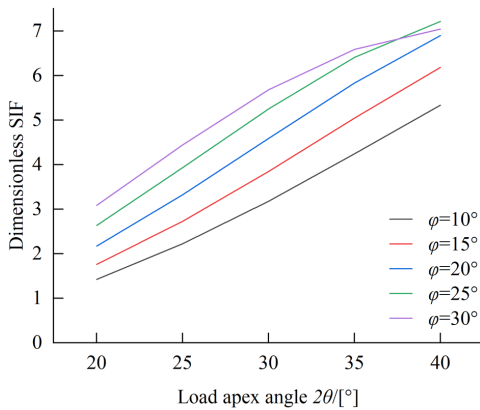**Fig. 10** The contact of the specimens to the spacer

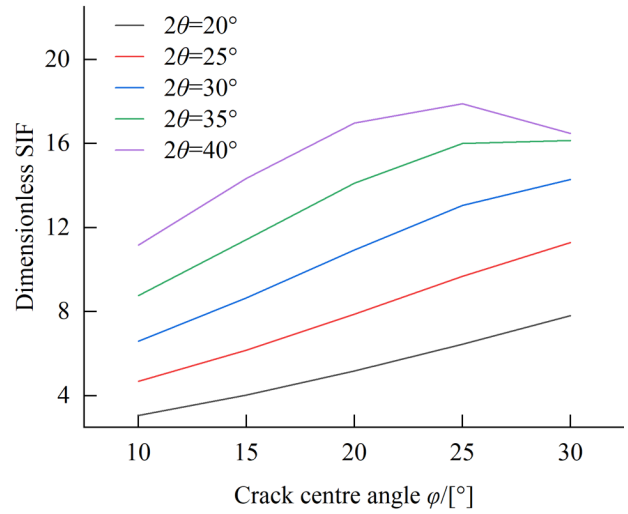**Fig. 11** Stress contour of simulation model with 40° loading apex angle and 30° crack center angle

(a)

(b)
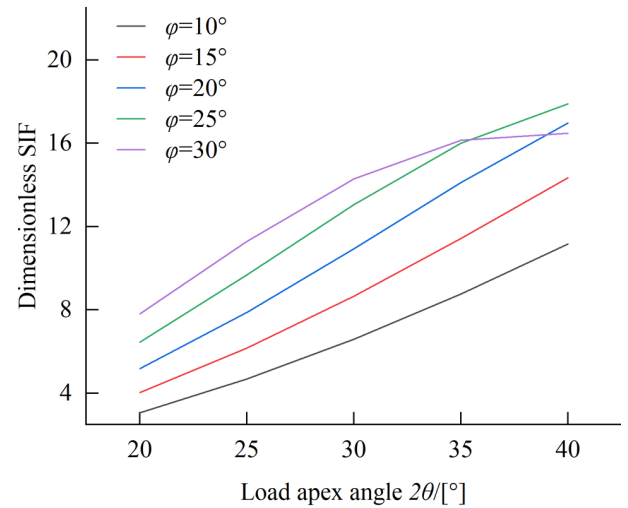
Fig. 12 Dimensionless SIF for model with h/R = 1/10 (a) dimensionless SIF varies with different φ values; (b) dimensionless SIF varies with different θ values

(a)

(b)

Fig. 13 Dimensionless SIF for model with h/R = 1/20 (a) dimensionless SIF varies with different φ values; (b) dimensionless SIF varies with different θ values

h/R = 1/10, 1/20, 1/30. Subfigure (a)s show the dimensionless SIF varies with different φ values for models with different θ values. Subfigure (b)s show how the dimensionless SIF varies with different θ values for models with different φ values. From all curves, the dimensionless SIFs show an increasing trend with the increase of both of φ and θ generally, as well as with the increase of thickness ratio h/R. For models with the same φ and θ, the model with a greater thickness has a higher dimensionless SIF.

Meanwhile, similar to the trend in Fig. 8 (c), the decrease in dimensionless SIF when θ is large enough is clearly shown in subfigure (b)s of Figs. 12, 13, and 14. The curves with crack angle of φ = 30° interest with the other curves. For different thickness ratios, the intersection points vary: the higher the thickness ratio, the larger the θ value at which the intersection occurs. For the other
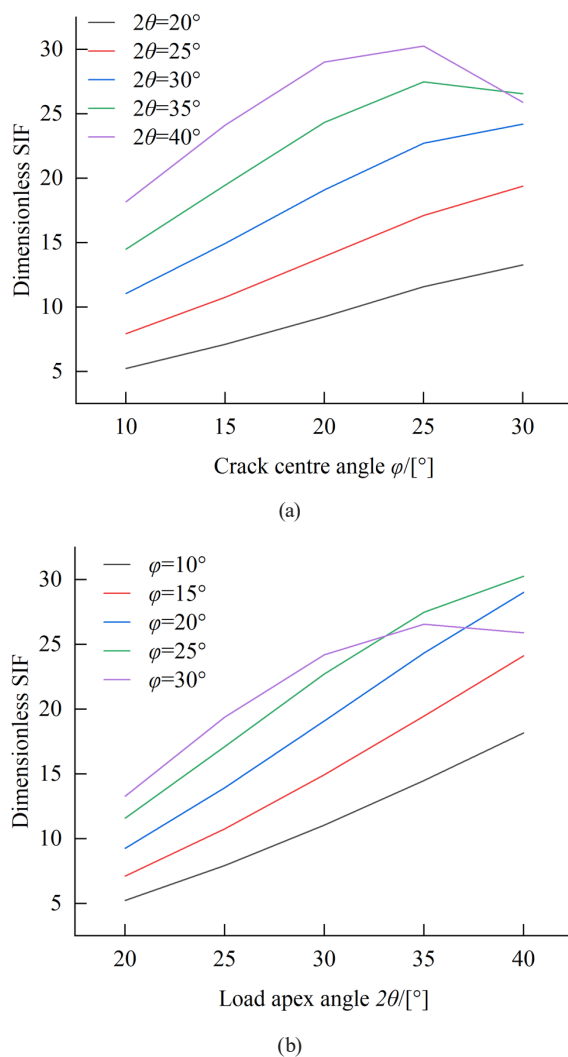
Fig. 14 Dimensionless SIF for model with $h/R = 1/30$ (a) dimensionless SIF varies with different φ values; (b) dimensionless SIF varies with different θ values

the suppression decrease with the increase in the thickness ratio. This means that there is a zone outside the load area where the increase in the dimensionless SIF can be suppressed or even decrease. For different thickness ratios, the thicker the model, the smaller the size of this zone.

6 Conclusions

Observing the SIF at the tip of the meridian cracks of the dome can help evaluate the fracture behavior of the dome. The calculation of the SIF for planar cracks, based on truncating the Williams' series expansion, can be extended to curved surface cracks using the equivalent plane transformation method. Through experiments and numerical simulations, the effects of dimensions, crack length, and distributed loading area on the SIF at the crack tip were studied. The results show,

1. the dimensionless SIFs show an increasing trend with the increase in crack length, distributed loading area and thickness ratio (thickness/ radius) generally.
2. The distributed load prevents any tension within the contact zone and suppresses top-surface radial cracking. The thicker the model, the more pronounced the effect. Within the bearing capacity, designing the loading edge to be wide can effectively inhibit the propagation of meridian cracks and increase the service life of the dome.

Conflict of interest statement

The authors declare no potential conflict of interest.

curves, the phenomenon where a larger loading can suppress the increasing trend of the dimensionless SIF also exists. As Fig. 14 (b) shows, the suppression of increasing trend of the $\varphi = 25°$ curve is evident, and the extent of

References

[1] Zavvar, E., Sadat Hosseini, A., Lotfollahi-Yaghin, M. A. "Stress concentration factors in steel tubular KT-connections with FRP-wrapping under bending moments", Structures, 33, pp. 4743–4765, 2021.
https://doi.org/10.1016/j.istruc.2021.06.100

[2] Zavvar, E., Giannini, G., Taveira-Pinto, F., Santos, P. R. "Parametric study of stress concentration factors in KT connections reinforced with concrete subjected to axial loads", Ocean Engineering, 298, 117209, 2024.
https://doi.org/10.1016/j.oceaneng.2024.117209

[3] Zavvar, E., Henneberg, J., Guedes Soares, C. "Stress concentration factors in FRP-reinforced tubular DKT joints under axial loads", Marine Structures, 90, 103429, 2023.
https://doi.org/10.1016/j.marstruc.2023.103429

[4] Zavvar, E., Hectors, K., De Waele, W. "Stress concentration factors of multi-planar tubular KT-joints subjected to in-plane bending moments", Marine Structures, 78, 103000, 2021.
https://doi.org/10.1016/j.marstruc.2021.103000

[5] Ahmadi, H., Zavvar, E. "Degree of bending (DoB) in offshore tubular KT-joints under the axial, in-plane bending (IPB), and out-of-plane bending (OPB) loads", Applied Ocean Research, 95, 102015, 2020.
https://doi.org/10.1016/j.apor.2019.102015

[6] Ahmadi, H., Zavvar, E. "The effect of multi-planarity on the SCFs in offshore tubular KT-joints subjected to in-plane and out-of-plane bending loads", Thin-Walled Structures, 106, pp. 148–165, 2016.
https://doi.org/10.1016/j.tws.2016.04.020

[7] Ahmadi, H., Zavvar, E. "Stress concentration factors induced by out-of-plane bending loads in ring-stiffened tubular KT-joints of jacket structures", Thin-Walled Structures, 91, pp. 82–95, 2015.
https://doi.org/10.1016/j.tws.2015.02.011

[8] Ahmadi, H., Yeganeh, A., Mohammadi, A. H., Zavvar, E. "Probabilistic analysis of stress concentration factors in tubular KT-joints reinforced with internal ring stiffeners under in-plane bending loads", Thin-Walled Structures, 99, pp. 58–75, 2016.
https://doi.org/10.1016/j.tws.2015.11.010

[9] Heyman, J. "Structural analysis: a historical approach", Cambridge University Press, 1998. ISBN 9780521622493
https://doi.org/10.1086/384344

[10] Walraven, J. C. "Fracture mechanics of concrete and its role in explaining structural behaviour", Taylor and Francis, 2007. ISBN 978-0-415-44617-4

[11] Michel, S., Sipos, A. A. "Fragmentation of inflated elastic brittle rings: Emergence of the quasi-equidistant spacing of cracks", Journal of the Mechanics and Physics of Solids, 179, 105372, 2023.
https://doi.org/10.1016/j.jmps.2023.105372

[12] Michel, S., Sipos, A. A. "On the cracking patterns of brittle rings with elastic radial support under hydrostatic pressure", Meccanica, 57(7), pp. 1639–1656, 2022.
https://doi.org/10.1007/s11012-022-01523-7

[13] Lancioni, G., Royer-Carfagni, G. "The variational approach to fracture mechanics. A practical application to the French Panthéon in Paris", Journal of Elasticity, 95, pp. 1–30, 2009.
https://doi.org/10.1007/s10659-009-9189-1

[14] Paris, P. C., Gomez, M. P., Anderson, W. E. "A rational analytic theory of fatigue", the Trend in Engineering, 13, pp. 9–14, 1961.

[15] Molent, L., Jones, R., Barter, S., Pitt, S. "Recent developments in fatigue crack growth assessment", International Journal of Fatigue, 28(12), pp. 1759–1768, 2006.
https://doi.org/10.1016/j.ijfatigue.2006.01.004

[16] Muskhelishvili, N. I. "Some basic problems of the mathematical theory of elasticity", Springer Dordrecht, 1977. ISBN 9789048182459
https://doi.org/10.1007/978-94-017-3034-1

[17] Williams, M. L. "On the stress distribution at the base of a stationary crack", Journal of Applied Mechanics, 24(1), pp. 109–114, 1957.
https://doi.org/10.1115/1.4011454

[18] Irwin, G. R. "Analysis of stresses and strains near the end of a crack traversing a plate", Journal of Applied Mechanics, 24(3), pp. 361–364, 1957.
https://doi.org/10.1115/1.4011547

[19] Vormwald, M., Hos, Y., Freire, J. L. F., Gonzáles, G. L. G., Díaz, J. G. "Crack tip displacement fields measured by digital image correlation for evaluating variable mode-mixity during fatigue crack growth", International Journal of Fatigue, 115, pp. 53–66, 2018.
https://doi.org/10.1016/j.ijfatigue.2018.04.030

[20] Vormwald, M., Hos, Y., Freire, J. L., Gonzáles, G. L., Díaz, J. G. "Variable mode-mixity during fatigue cycles – crack tip parameters determined from displacement fields measured by digital image correlation", Frattura ed Integrità Strutturale, 11(41), pp. 314–322, 2017.
https://doi.org/10.3221/IGF-ESIS.41.42

[21] Camacho-Reyes, A., Vasco-Olmo, J. M., James, M. N., Diaz, F. A. "Characterization of non-planar crack tip displacement fields using a differential geometry approach in combination with 3D digital image correlation", Fatigue and Fracture of Engineering Materials and Structures, 45(5), pp. 1521–1536, 2022.
https://doi.org/10.1111/ffe.13686

[22] Cao, S., Sipos, A. A. "About measuring the stress intensity factor of cracks in curved, brittle shells", Frattura ed Integrità Strutturale, 18(69), pp. 1–17, 2024.
https://doi.org/10.3221/IGF-ESIS.69.01

[23] Ewing, P. D., Williams, J. G. "The fracture of spherical shells under pressure and circular tubes with angled cracks in torsion", International Journal of Fracture, 10, pp. 537–544, 1974.
https://doi.org/10.1007/BF00155256

[24] Liu, W., Yue, Z., Yang, G. "Experimental investigation of a circumferential crack in a PMMA cylindrical shell using caustics", Polymer Testing, 79, 106086, 2019.
https://doi.org/10.1016/j.polymertesting.2019.106086

[25] Qasim, T., Ford, C., Bush, M. B., Hu, X., Malament, K. A., Lawn, B. R. "Margin failures in brittle dome structures: relevance to failure of dental crowns", Journal of Biomedical Materials Research Part B: Applied Biomaterials, 80B(1), pp. 78–85, 2007.
https://doi.org/10.1002/jbm.b.30571

[26] Cao, S., Sipos, A. A. "Cracking patterns of brittle hemispherical domes: an experimental study", Frattura ed Integrità Strutturale, 16(59), pp. 265–310, 2022.
https://doi.org/10.3221/IGF-ESIS.59.20

[27] Correlated Solutions, Inc. "VIC-Snap, (version 9)", [computer program] Available at: https://www.correlatedsolutions.com/vic-3d [Accessed: 15 January 2025]

[28] Howell, P., Kozyreff, G. Ockendon, J. "Applied solid mechanics", Cambridge University Press, 2008. ISBN 9780511611605
https://doi.org/10.1017/CBO9780511611605

[29] Dassault Systèmes "Abaqus, (2022)", [computer program] Available at: https://www.3ds.com/products/simulia/abaqus [Accessed: 15 January 2025]

[30] Schiaretti, M., Cai, J., Jiang, X., Zhang, S., Schott, D. "A numerical investigation of an abnormal phenomenon of stress intensity factor (SIF) in a cracked T-Butt joint accounting for welding effect", Journal of Marine Science and Application, 20(2), pp. 343–353, 2021.
https://doi.org/10.1007/s11804-021-00199-x

[31] Eskandari, H., Ghanbari, M., Mirzadeh, F. "Three-dimensional stress analysis for semi-elliptical cracks in the connection of cylinder-hemispherical head for thick-walled cylindrical pressure vessels", Journal of Solid Mechanics, 13(1), pp. 1–10, 2021.
https://doi.org/10.22034/jsm.2020.555468.1194

[32] Hu, H., Chen, D. "Uncertainty qualification in evaluating dynamic and static stress intensity factors using SBFEM based on model order reduction", Engineering Fracture Mechanics, 288, 109349 2023.
https://doi.org/10.1016/j.engfracmech.2023.109349

[33] Aliha, M. R. M., Ziari, H., Mojaradi, B., Sarbijan, M. J. "Modes I and II stress intensity factors of semi-circular bend specimen computed for two-phase aggregate/mastic asphalt mixtures", Theoretical and Applied Fracture Mechanics, 106, 102437, 2020.
https://doi.org/10.1016/j.tafmec.2019.102437